

Analyst

Accepted Manuscript



This is an *Accepted Manuscript*, which has been through the Royal Society of Chemistry peer review process and has been accepted for publication.

Accepted Manuscripts are published online shortly after acceptance, before technical editing, formatting and proof reading. Using this free service, authors can make their results available to the community, in citable form, before we publish the edited article. We will replace this *Accepted Manuscript* with the edited and formatted *Advance Article* as soon as it is available.

You can find more information about *Accepted Manuscripts* in the [Information for Authors](#).

Please note that technical editing may introduce minor changes to the text and/or graphics, which may alter content. The journal's standard [Terms & Conditions](#) and the [Ethical guidelines](#) still apply. In no event shall the Royal Society of Chemistry be held responsible for any errors or omissions in this *Accepted Manuscript* or any consequences arising from the use of any information it contains.

Parts Per Billion Detection of Uranium with a Porphyrinoid-containing Nanoparticle and *in vivo* Photoacoustic Imaging

I-Ting Ho^a, Jonathan L. Sessler^a, Sanjiv Sam Gambhir^{b,c}, and Jesse V. Jokerst^{b,#}

^aDepartment of Chemistry
The University of Texas at Austin
105 E. 24th Street-A5300
Austin, TX 78712-1224

^bMolecular Imaging Program at Stanford (MIPS)
Department of Radiology
318 Campus Drive
Stanford University School of Medicine
Stanford, CA 94305-5427

^cBioengineering, Materials Science, and Engineering
Stanford University
Stanford, CA 94305

[#] Address effective July 1, 2015:
Department of NanoEngineering
University of California, San Diego
jjokerst@eng.ucsd.edu

Keywords: Photoacoustic Imaging, Porphyrinoid Macrocycles, Activatable Nanoparticle, Dosimetry

Abstract

Chemical tools that can report radioactive isotopes would be of interest to the defense community. Here we report ~250 nm polymeric nanoparticles containing porphyrinoid macrocycles with and without pre-complexed depleted uranium and demonstrate that the latter species may be detected easily and with high sensitivity *via* photoacoustic imaging. The porphyrinoid macrocycles used in the present study are non-aromatic in the absence of the uranyl cation, but aromatic after cation complexation. We solubilized both the freebase and metalated forms of the macrocycles in poly(lactic-co-glycolic acid) and found a peak in photoacoustic signal at 910 nm excitation in the case of the uranyl complex. The signal was stable for at least 15 minutes and allowed detection of uranium concentrations down to 6.2 ppb (5.7 nM) *in vitro* and 0.57 ppm (19 fCi; 0.52 μ M) *in vivo*. To the best of our knowledge, this is the first report of a nanoparticle that detects an actinide cation via photoacoustic imaging.

Statement of Novelty: To the best of our knowledge, this is the first report of a nanoparticle that detects an actinide cation via photoacoustic imaging.

1
2
3
4 Defense and energy-related agencies have an urgent need for chemical tools that can identify,
5 sequester, and quantitate dangerous radioisotopes *in vivo*. While wearable dosimetry badges
6 are an important and affordable tool to measure cumulative exposure over a defined time
7 period^{1, 2}, they cannot be used to image the *in vivo* distribution of the contamination. Handheld
8 Geiger counting is an important approach to identifying contamination sites and allows
9 detection of alpha and beta particles as well as gamma radiation. However, Geiger counters
10 cannot differentiate between different types of ionizing radiation or identify the isotope
11 producing the radiation¹. Furthermore, this approach is not amenable to *in vivo* imaging nor
12 does it assess the *in vivo* biodistribution of contamination in a living subject. An alternative
13 approach involves the use of gamma cameras. While these tools provide for powerful clinical
14 imaging and can be used at the point of care to measure gamma irradiation³, they suffer from
15 low spatial (cm) and temporal resolution (minutes), but with sensitivity via single photon
16 emission computed tomography of $10^{-10} - 10^{-11} \text{ M}^4$.

17
18
19
20 One alternative is photoacoustic imaging, which is an acoustic detection modality that converts
21 incident light pulses into pressure differences via thermal expansion⁴⁻⁹. Photoacoustics
22 combines the depth of penetration and temporal/spatial resolution of traditional backscatter-
23 mode (B-mode) ultrasound with the high contrast and spectral behavior of optical imaging.
24 Photoacoustics has been used to characterize materials^{10, 11} and has been applied for a variety
25 of cancer¹²⁻¹⁶ and cell imaging^{17, 18} applications. Here we suggest that photoacoustics used in
26 tandem with an appropriate molecular imaging contrast agent could determine actinide
27 concentrations *in vivo* following radiation exposure.

28
29
30
31 Before the widespread adoption of inductively coupled plasma mass spectrometry (ICP-MS)
32 for the analysis of heavy metals, photoacoustic spectroscopy was one of many analytical
33 techniques under investigation as a quantitative tool for the analysis of environmental
34 samples^{19, 20}. In one report from 1983, U^{VI} as $\text{UO}_2\text{SO}_4 \cdot 3\frac{1}{2} \text{H}_2\text{O}$ concentrations above $1 \mu\text{M}$
35 were measured in an aqueous solution with a customized cuvette¹⁹. While these *in vitro*
36 studies illustrated the principle of uranium measurements with photoacoustics, they were only
37 possible because the samples were dissolved in concentrated nitric acid. Furthermore, the
38 absorption peak for U^{VI} (420 nm) is markedly blue-shifted relative to the “optical window”
39 considered optimal for biological imaging (700-1000 nm)^{4, 5}. Thus, the literature has long been
40 silent on the topic of using photoacoustics for measuring this radioisotope. To the best of our
41 knowledge, there have no *in vivo* detection studies.

42
43
44
45 We report here an important first step towards achieving the long-term goal of using
46 photoacoustics to detect uranium and other radioisotopes *in vivo*. Specifically, we describe a
47 new class of nanoparticles based on embedded porphyrinoid molecules and show that these
48 species produce an easy-to-detect photoacoustic signal when the porphyrinoid contains a pre-
49 complexed uranyl cation but not in its absence. The porphyrinoid analogue used for this study,
50 cyclo[1]furan[1]pyridine[4]pyrrole (“F1P1P4”), has electronic features that are highly dependent
51 on its coordination environment, displaying nonaromatic and aromatic features in its freebase
52 and uranyl cation complexed forms, respectively²¹. We thus hypothesized that these
53 aromaticity changes could be harnessed to quantitate uranyl via photoacoustic imaging.
54 Porphyrin-like structures^{22, 23} have a long history of use in medicine including as sensitizers for
55
56
57
58
59
60

1 radiation therapy^{24, 25}, photodynamic therapy^{26, 27}, and as imaging agents^{24, 28, 29}. Thus, their
2 reconfiguration for defense imaging applications may face a lower barrier to use in humans
3 than might otherwise be expected.
4
5

6 The metalated and freebase forms of F1P1P4 were independently stabilized in a polymer
7 nanoparticle. After nanoparticle characterization, we studied the spectral behavior and
8 detection limits of the resulting materials. This approach is unique in that the photoacoustic
9 signal is entirely dependent on the uranyl cation—no detectable signal was obtained for the
10 metal-free system. This nanoparticle increases the absorptivity of the uranyl ions, and to the
11 best of our knowledge, represent the first example of *in vivo* imaging of a radioisotope
12 surrogate using photoacoustics. Long term, we envision a collection of porphyrinoid
13 nanoparticles each with a unique selectivity for an isotope of interest as a means of detecting
14 the presence of a specific radio-hazard.
15
16
17
18
19
20
21
22
23
24
25
26
27
28
29
30
31
32
33
34
35
36
37
38
39
40
41
42
43
44
45
46
47
48
49
50
51
52
53
54
55
56
57
58
59
60

Methods

Nanoparticle Synthesis. The hybrid macrocycle, cyclo[1]furan[1]pyridine[4]pyrrole (ligand), as well as its uranyl-containing analogue (complex), were synthesized as described previously²¹. The free F1P1P4 macrocycle and its uranyl complex were dissolved to produce 2 mg/mL solutions in acetone and dichloromethane (DCM), respectively. Then, 200 μ L of this organic phase was added to 1 mL of a 25 mg/mL solution of acid-terminated poly(lactic-co-glycolic) acid (PLGA) in DCM. The combined organic mixture was added dropwise to 25 mL of a 0.3% solution of polyvinyl alcohol in water with sonication (Sonifier 150, Branson Corp). The resulting mixture was sonicated for an additional 2 minutes followed by rotary evaporation to yield PLGA nanoparticles (NPs). ²³⁵U-depleted uranium was used throughout. Gold nanorods for comparison were made using the seeded growth method described previously^{30, 31}.

Characterization. Size and surface charge were measured using dynamic light scattering (DLS) and a ZetaSizer-90 (Malvern) instrument, respectively. Inductively coupled plasma-mass spectrometry (ICP-MS) was used to quantitate uranium with NIST-calibrated standards (Inorganic Ventures). To prepare the NPs for analysis, they were dissolved in glacial nitric acid with sonication and then diluted to 5% nitric acid in doubly deionized (DDI) water. All transmission electron microscopy (TEM) and energy-dispersive X-ray spectroscopy (EDS) was performed with a Tecnai G2 X-Twin (FEI Co.) instrument operating at 200 kV.

Photoacoustic Imaging. Photoacoustic imaging was performed with a LAZR commercial instrument (Visualsonics) equipped with a 21 MHz-centered transducer as described previously^{17, 32}. The system uses a flashlamp pumped Q-switched Nd:YAG laser with an optical parametric oscillator and a second harmonic generator operating at 20 Hz between 680 and 970 nm with a 1 nm step size and 4-6 ns pulses. The peak energy is 45 ± 5 mJ at 20 Hz at the source. The spot size is 1 mm x 24 mm and the full field of view is 14-23 mm wide. The acquisition rate is 5 frames per second. Photoacoustic data was quantitated with ImageJ³³ using the integrated density function in defined regions of interested. These bit depth values were considered to be arbitrary units (a.u.). Data were considered significant when the two-tailed t test produced a p value greater than 0.05.

Animal Studies. Female nu/nu mice (6-16 weeks old) were used in this study in triplicate at each datum point. All animal work was conducted in accordance with the Administrative Panel on Laboratory Animal Care at Stanford University. Prior to imaging, mice were anesthetized with 2% isoflurane in house oxygen at 2 L/min as confirmed by tail pinch. A 100 μ L bolus of the nanoparticles was injected subcutaneously and imaged 15 minutes after injection. For validation studies, animals were sacrificed with CO₂, and the implanted nanoparticle bolus analyzed by dissection.

Results and Discussion

A primary goal was to confirm that uranyl-containing porphyrinoid complexes will indeed produce photoacoustic signal. Towards this end, we dissolved both the ligand (**Fig. 1A**) and complex (**Fig. 1B**) in organic solvents at 1 mg/mL each and sealed them inside an agar phantom. The photoacoustic spectra were collected for each (**Figure 1C**). The complex produced a peak signal at 848 nm, which matches nicely the 847 absorption peak seen in prior work and which is ascribed to the conjugated ($4n + 2$) π -electron aromatic character of the molecule²¹. The ligand produced no photoacoustic signal. In fact, the uranyl complex had a signal that was 50- to 250-fold higher than the ligand alone, being 234 ± 17 -fold higher over the 826 – 860 nm spectral region near the dominant absorption peak of the complex.

One limitation to using these porphyrinoids *in vivo* is their poor solubility in aqueous media. To overcome this limitation, we incorporated both the ligand and the complex into PLGA nanoparticles^{34, 35} and characterized them with TEM (**Fig. 1D**) and DLS (**Fig. 2A**). The average size by TEM was 334.7 ± 36.0 nm. By DLS, the ligand-NP was 218.4 ± 5.3 nm and the complex-NP was 218.1 ± 8.6 nm; the polydispersity indices (**PDI**) were all below 0.125. The surface charge was -30.1 ± 0.9 mV for the ligand-NPs and -23.9 ± 0.6 mV for the complex NPs. Batch-to-batch reproducibility in size for 4 batches was less than 2% (**Fig. 2B**). We further characterized the complex-containing PLGA NPs (complex-NPs) by drying a known volume to constant weight. The dry weight concentration was 5.5 mg/mL. We used the density of hydrated PLGA and the volume of a 250 nm NP (8.2×10^6 nm³ or 8.2×10^{-15} cm³) to calculate a molar concentration of 0.76 nM nanoparticles. The contribution of the complexes to the density is <0.5% and was thus not considered in the calculations.

We also measured the effect of time on nanoparticle stability. The DLS histograms for ligand- and complex-NPs after one month of storage on the benchtop were compared to the histograms collected immediately after synthesis (**Fig. 2C**). The ligand-NPs had a dramatic change in PDI—0.12 after synthesis and 0.66 one month after synthesis. The peak of the ligand-NPs also shifted to ~2300 nm. In contrast, the complex-NPs showed little change in either PDI or peak location (**Fig. 2C**). This may be because of the charge stabilizing effects the uranyl complex has on the PLGA nanoparticle.

FIGURE 1

Figure 1. Contrast Agent Design and Characterization. **A)** The porphyrinoid macrocycle cyclo[1]furan[1]pyridine[4]pyrrole (“ligand”) lacks full peripheral conjugation in the absence of a uranyl cation. **B)** On the other hand, the uranyl complex displays aromatic character as reflected in the $4n + 2$ π -electron periphery (shown with the darker lines). **C)** The metal-free ligand (red line) produces no detectable photoacoustic signal. In contrast, the uranyl complex gives rise to a photoacoustic signal with a peak near 850 nm (blue line). This peak shifts to 910 when the complex is placed inside PLGA nanoparticles (black line). **Inset:** photograph of the ligand dissolved in acetone (yellow) and the uranyl complex dissolved in dichloromethane (green). **D)** Both the ligand and the complex are very hydrophobic and were placed inside PLGA nanoparticles to increase hydrophilicity. Panel **D** shows TEM images of these nanoparticles.

FIGURE 2

Figure 2. Nanoparticle Size Reproducibility and Stability. **A)** Dynamic light scattering data for freshly prepared ligand-NPs and complex-NPs, both with peaks near 220 nm. **B)** Four replicate batches of complex-NPs were made with bath-to-batch variation below 2%. Error bars in panel B represent the standard deviation of 3 replicate DLS runs. **C)** DLS analysis was repeated on nanoparticles after storage on the bench for one month. The complex-NPs showed little change, but the ligand-NPs had a dramatic increase in PDI and size. This indicates degradation of the NP.

We next dissolved known amounts of the complex-containing nanoparticles (complex-NPs) in glacial nitric acid with bath sonication and used ICP-MS to measure the uranium concentration. The value obtained, 5.7 ± 0.7 ppm, corresponds to 29,000 uranyl groups per NP. Finally, we recorded the photoacoustic spectrum of the complex-NPs at 0.25 nM. The photoacoustic signal for the complex-NPs (peak maximum at 910 nm) was red-shifted relative to what is seen in organic media (peak maximum at 848 nm; **Fig. 1C**). This shift is ascribed to π - π donor-acceptor interactions within the hydrophilic nanoparticle that are not present in organic media.

FIGURE 3

Figure 3. Photoacoustic detection limits for the complex-NPs. **A)** Decreasing concentrations of the complex-NPs were placed inside plastic tubing and sealed within an agar phantom from left to right. Both B-mode (black and white) and photoacoustic mode (red) imaging was performed. **B)** Quantitation of the imaging data revealed a U dose dependence and a plateau above 1 ppm uranium. This regime is the equivalent of $5.2 \mu\text{M} - 0.052 \mu\text{M}$ uranium chelate. **C)** Plot of the lower region of the graph in B, showing the linear behavior ($R^2 > 0.99$) at and below 150 ppb uranium. The calculated limit of detection is 6.2 ppb. In both panels B and C, the red error bars represent the standard deviation. The scale bar in **A** represents 5 mm.

We next measured the photoacoustic signal of decreasing concentrations of complex-NPs in a phantom (**Fig. 3A**). NPs at concentrations ranging from 5.5 to 0.055 mg/mL (5700 – 57 ppb or 0.76 – 0.0076 nM NPs or $5.2 \mu\text{M} - 0.052 \mu\text{M}$ uranium chelate) were placed inside plastic tubes using normal saline as the diluent. These tubes were then sealed beneath agar and imaged at 910 nm. Linear behavior ($R^2 > 0.96$) was noted through 1.1 mg/mL (1140 ppm; **Fig 3B**). The lowest concentration we measured had photoacoustic signal 15.3-fold higher than the blank ($p < 0.001$; **Fig 3C**). Using 3 standard deviations above the background, we calculated a theoretical limit of detection of 6.2 ppb uranium. When this 6.2 ppb sensitivity was converted to molarity via the 1092.35 g/mol molecular weight of chelated uranium, the detection limit is 5.7 nM uranium. While this is higher than the parts-per-trillion detection limits that can be attained using ICP-MS³⁶, it is lower (i.e., superior) to complexometric methods³⁷ or atomic absorption spectroscopy. Most important is that this imaging approach can be performed *in vivo* as detailed below.

We tested the *in vivo* sensitivity of our system by implanting 100 μL boluses of complex-NPs into healthy mice ($n = 3$) with a 50% matrigel carrier (**Fig. 4A**). We imaged with 910 nm excitation and a 21 MHz center frequency transducer. The photoacoustic signal-to-background was 7.4 for the highest concentration (0.35 nM NPs, 2.85 ppm uranium). The lowest concentration detectable versus sham injection was 570 ppb uranium (0.076 nM nanoparticles; **Fig. 5A**) and had photoacoustic signal 1.8-fold higher than the sham injection ($p < 0.05$). The

1
2 relationship between uranium concentration and dose was linear at $R^2 > 0.94$. When this 570
3 ppb value was converted to molarity via the 1092.35 g/mol molecular weight of chelated
4 uranium, the sensitivity is 0.52 μM . To better frame this concentration, we converted the $5.7 \times$
5 10^{-8} g mass value to activity (assuming pure U^{238}) using the 3.36×10^{-7} Ci/g U^{238}
6 specific activity³⁸. The value of 19 fCi is well below the detection limits of gamma cameras and is even
7 lower than background radiation.
8

9
10 The *in vivo* imaging data were validated with ICP-MS, which showed that the bolus of uranium
11 complex NPs had 800-fold more uranium than the corresponding bolus containing the metal-
12 free form of the macrocycle. The injection procedure could cause trauma (hematoma) that
13 might artificially increase the photoacoustic signal. To determine whether that was the case,
14 we implanted a 100 μL bolus of 0.38 nM ligand-NPs into mice (**Fig. 4B**). No increase in
15 photoacoustic signal was seen in these mice.
16

17
18 Finally, we compared the stability of the photoacoustic signal from complex-NPs to that from
19 gold nanorods (GNRs) on an isomolar basis. The molar concentration of the GNRs were
20 estimated using published molar extinction coefficients³⁹. The molar concentration of the PLGA
21 used the size and density. The complex-NPs gave rise to a 2.6-fold stronger signal than gold
22 nanorods at isomolar values and with the wavelengths optimized for each nanoparticle type.
23 That is, we imaged complex-NPs at 910 nm and the GNRs at 733 nm—their respective peak
24 absorptions. Upon continuous imaging at these respective peak wavelengths, there was no
25 significant change in photoacoustic signal intensity even after 15 minutes of continuous
26 illumination in the case of the complex-NPs. In contrast, the signal from the GNRs decreased
27 by 40% over this same period because of deformation under irradiation (**Fig. 5B**)⁴⁰.
28
29

30
31 Other advantages of this approach include the 5 Hz acquisition rate and the 2 to 5 cm
32 penetration depth of photoacoustic imaging. We show more than 2 log orders of improvement
33 in detection limits versus photoacoustic spectroscopy^{19, 20}. This increase is ascribed to the
34 increased molar absorptivity provided by the use of conjugated macrocycles. Typically, uranyl
35 cations display molar absorptivity values between $10\text{-}30 (\text{M cm})^{-1}$, depending on the
36 wavelength, solvent, counter-ions, etc.^{19, 41}. In contrast, the uranyl-complexed form of the
37 porphyrinoid macrocycle described here has a molar absorptivity of $18,100 (\text{M cm})^{-1}$ at 847
38 nm²¹. This approach also offers an excitation peak in the heart of the optical window (910 nm).
39 While spectroscopy has suggested a peak at 650 nm for U^{IV} as $\text{UO}_2(\text{NO}_3)_2 \cdot 6\text{H}_2\text{O}$ ¹⁷, this
40 oxidation state has limited stability⁴².
41
42

43
44 The stability and selectivity of the complex was assessed previously²¹. Here, the uranyl
45 complex was incubated with a 10-fold molar excess of 8 different metal ion salts followed by a
46 reflux for 24 hours. Of the 8 samples, appreciable changes to the spectra were only noted for
47 SnCl_2 , CuCl_2 , and $\text{Th}(\text{NO}_3)_4$. This may be due to decomposition of the uranium complex or
48 metal ion replacement. One approach to modifying the selectivity is by tuning the $\sim 10 \text{ \AA}$
49 pore size of the PLGA nanoparticle⁴³. Larger pores have been created on PLGA nanoparticles with
50 H_2O_2 ⁴⁴ or ammonium bicarbonate⁴⁵ and may allow increased penetration of uranyl. Smaller
51 pores could be created by tuning the molecular weight of the polymer. Thus, a pore size
52 optimal for uranyl could be created that physically excludes the larger competing species.
53
54
55
56
57
58
59
60

1
2 One limitation of the present proof-of-concept study is that it relies on the use of a preformed
3 uranyl complex. The uranyl chelation does not occur in real time *in vivo* under the conditions of
4 analysis. Current synthetic effort is thus focused on creating porphyrinoids that are both water-
5 soluble and which can complex radioisotopes *in vivo*.
6

7
8 Future studies with the present system may explore the use of other IR peaks in the second
9 optical window⁴⁶. The uranyl complex used here also displays a strong peak at 1177 nm in
10 organic media that could be used for second NIR window imaging. While the nanoparticle
11 formulation would also likely red-shift this peak, this spectroscopic feature could also be
12 exploited for photoacoustic imaging with the appropriate laser excitation sources. This is
13 expected to allow a greater depth of penetration for the excitation radiation. In addition, using
14 two wavelengths and a dual wavelength imaging setup might also increase sensitivity via
15 ratiometric imaging to compensate for background signal.
16
17
18
19

20 FIGURE 4

21
22 **Figure 4. *In vivo* Imaging.** Panels on the left are backscatter (B-mode) ultrasound images, and panels on the
23 right present photoacoustic data (red). In panel **A**, a 100 μ L bolus of 0.38 nM (2.75 mg/mL) complex-NPs in 50%
24 matrigel was injected subcutaneously and imaged 15 minutes later. Panel **B** corresponds to the uranium-free NP
25 control. In both panels, the green dashed signal highlights the injection site and the scale bar and intensity scale
26 designators apply to both the B-mode image and the photoacoustic panel.
27
28

29 FIGURE 5

30
31 **Figure 5. *In vivo* Sensitivity and Stability. A)** Decreasing concentrations (2.6 – 0.52 μ M uranium complex or
32 2.85 – 0.57 ppm uranium) of complex-NPs were implanted subcutaneously and imaged with photoacoustics. The
33 response was linear with $R^2 = 0.94$. The * designator indicates significance versus the 0 mg/mL control with
34 $p < 0.01$. **B)** Equimolar concentrations of complex-NPs and gold nanorods (GNRs) were imaged continuously for
35 15 minutes. There is no decrease in NP signal, but GNRs show a 40% decrease due to morphology changes from
36 the excitation fluence.
37
38
39
40
41
42
43
44
45
46
47
48
49
50
51
52
53
54
55
56
57
58
59
60

Conclusion

Despite an abundance of reports on porphyrin-based photoacoustic imaging^{28, 29, 47, 48}, to the best of our knowledge, this is the first example wherein porphyrinoids are combined with photoacoustic imaging to quantify a specific test actinide cation. The present study also illustrates the utility of the macrocycle-based NPs for photoacoustic molecular imaging in conjunction with B-mode to obtain anatomic information. We plan to explore other macrocyclic systems, including those with specificity for biologically important cations, such as calcium, magnesium, mercury, and lead, in an effort to monitor disease- and toxicity-related concentrations. Formulating chelating macrocycles with cyclodextrins may also provide for real-time scavenging of various ions *in vivo* in addition to photoacoustic imaging⁴⁹.

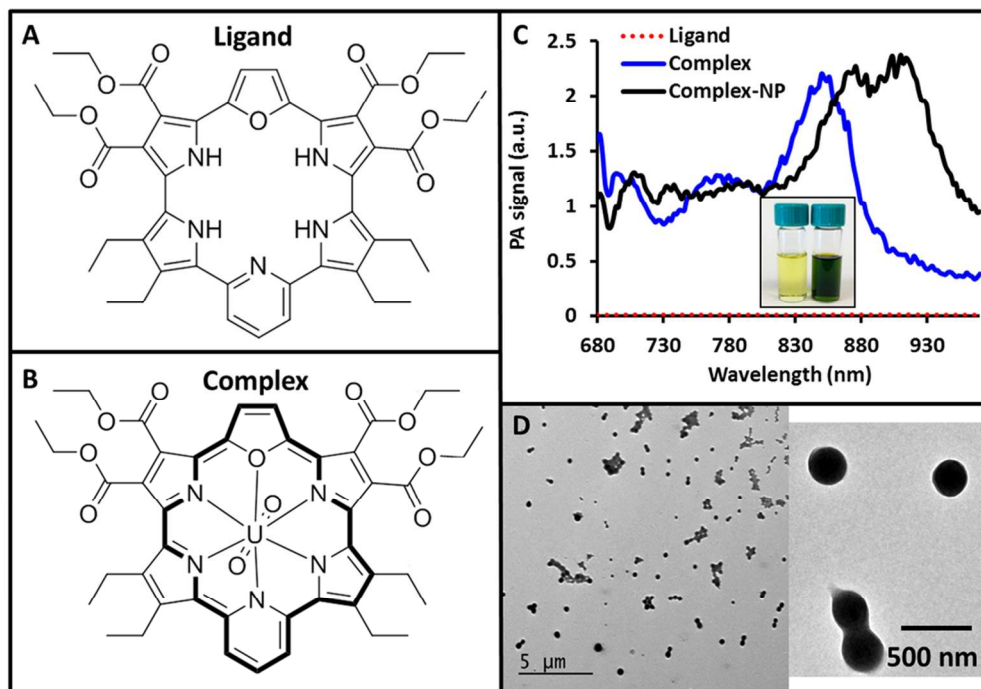
Acknowledgements

JVJ acknowledges support from NHLBI (HL117048). Instrumentation used in this work was supported by NIH grant S10-OD010344. Support for infrastructure and TEM imaging was provided by NIH grants U54-CA151459 and P50-CA114747 (SSG). The work in Austin was supported by the U.S. Department of Energy (DOE) Office of Basic Energy Sciences (Grant DE-FG02-01ER15186 to JLS).

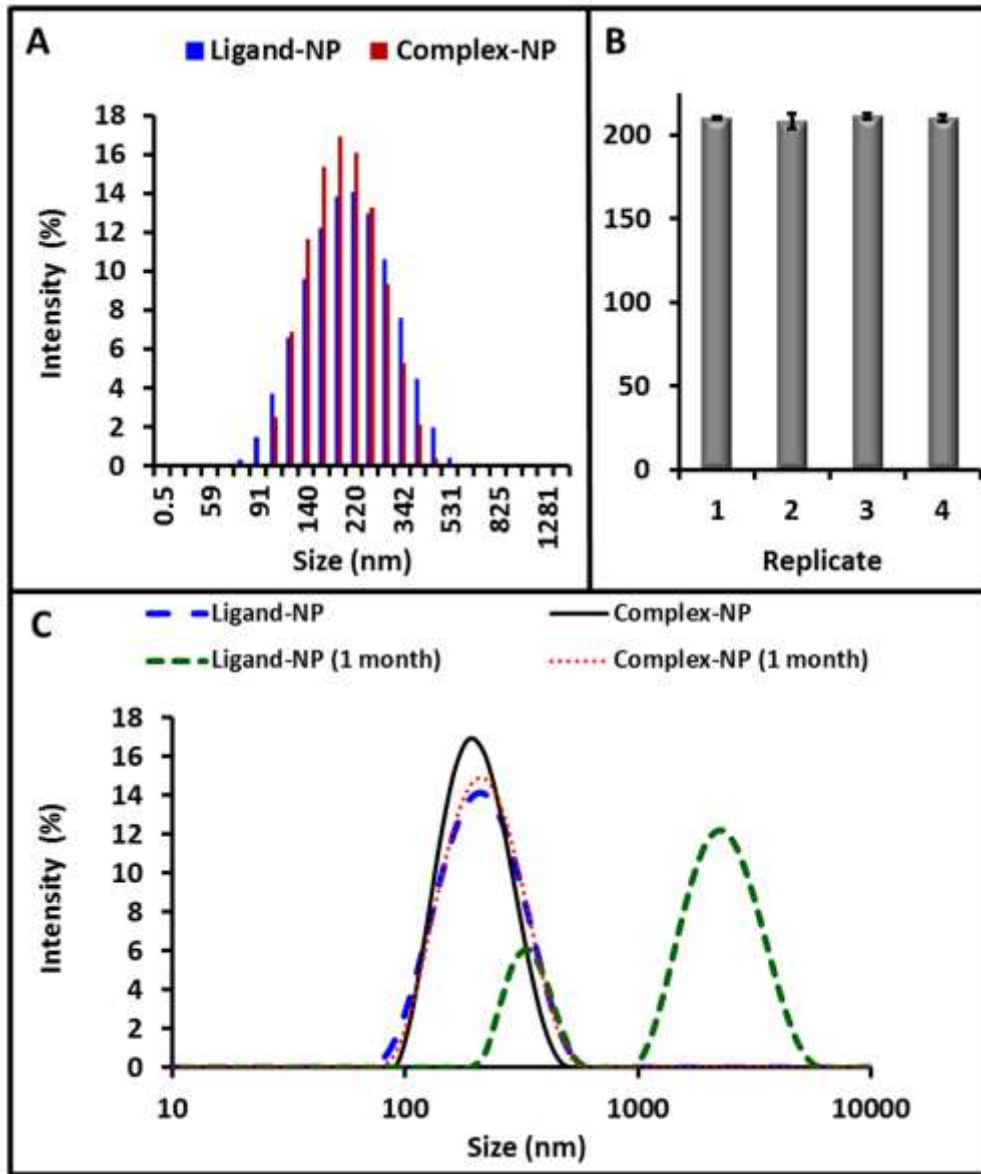
References

1. G. F. Knoll, *Radiation Detection and Measurement*, John Wiley & Sons, 2010.
2. W. L. McLaughlin, A. Boyd, K. Chadwick, J. McDonald and A. Miller, *Dosimetry for Radiation Processing*, Taylor and Francis, 1989.
3. S. Kawatsuma, M. Fukushima and T. Okada, *Industrial Robot: An International Journal*, 2012, **39**, 428-435.
4. M. L. James and S. S. Gambhir, *Physiological Rev.*, 2012, **92**, 897-965.
5. L. V. Wang and S. Hu, *Science*, 2012, **335**, 1458-1462.
6. V. Ntziachristos and D. Razansky, *Chem. Rev.*, 2010, **110**, 2783-2794.
7. D. Razansky, M. Distel, C. Vinegoni, R. Ma, N. Perrimon, R. W. Koster and V. Ntziachristos, *Nat. Photon.*, 2009, **3**, 412-417.
8. K. Pu, A. J. Shuhendler, J. V. Jokerst, J. Mei, S. S. Gambhir, Z. Bao and J. Rao, *Nat. Nano.*, 2014, **9**, 233-239.
9. K. Cheng, S.-R. Kothapalli, H. Liu, A. L. Koh, J. V. Jokerst, H. Jiang, M. Yang, J. Li, J. Levi and J. C. Wu, *J. Am. Chem. Soc.*, 2014, **136**, 3560-3571.
10. A. Rosencwaig, *Photoacoustics and Photoacoustic Spectroscopy*, Wiley, 1980.
11. R. A. Kruger, *Med. Phys.*, 1994, **21**, 127-131.
12. R. A. Kruger, C. M. Kuzmiak, R. B. Lam, D. R. Reinecke, S. P. Del Rio and D. Steed, *Med. Phys.*, 2013, **40**, 113301.
13. A. De la Zerda, C. Zavaleta, S. Keren, S. Vaithilingam, S. Bodapati, Z. Liu, J. Levi, B. R. Smith, T. J. Ma, O. Oralkan, Z. Cheng, X. Chen, H. Dai, B. T. Khuri-Yakub and S. S. Gambhir, *Nat. Nano.*, 2008, **3**, 557-562.
14. M. F. Kircher, A. de la Zerda, J. V. Jokerst, C. L. Zavaleta, P. J. Kempen, E. Mittra, K. Pitter, R. Huang, C. Campos and F. Habte, *Nat. Med.*, 2012, **18**, 829-834.
15. Y. S. Chen, W. Frey, S. Kim, P. Kruizinga, K. Homan and S. Emelianov, *Nano Lett.*, 2011, **11**, 348-354.
16. A. Agarwal, S. Huang, M. O'Donnell, K. Day, M. Day, N. Kotov and S. Ashkenazi, *J. Appl. Phys.*, 2007, **102**, 064701-064701-064704.
17. J. V. Jokerst, M. Thangaraj, P. J. Kempen, R. Sinclair and S. S. Gambhir, *ACS Nano*, 2012, **6**, 5920-5930.
18. E. I. Galanzha, E. V. Shashkov, T. Kelly, J.-W. Kim, L. Yang and V. P. Zharov, *Nat. Nano.*, 2009, **4**, 855-860.
19. W. Schrepp, R. Stumpe, J. Kim and H. Walther, *Appl. Phys. B*, 1983, **32**, 207-209.
20. T. Kimura, G. Serrano, S. Nakayama, K. Takahashi and H. Takeishi, *Radiochimica Acta*, 1992, **58**, 173-178.
21. I.-T. Ho, Z. Zhang, M. Ishida, V. M. Lynch, W.-Y. Cha, Y. M. Sung, D. Kim and J. L. Sessler, *J. Am. Chem. Soc.*, 2014, **136**, 4281-4286.
22. T. M. Chang, S. Sinharay, A. V. Astashkin and E. Tomat, *Inorg. Chem.*, 2014, **53**, 7518-7526.
23. J. L. Sessler and S. J. Weghorn, *Expanded, Contracted and Isomeric Porphyrins*, Elsevier, 1997.
24. S. W. Young, F. Qing, A. Harriman, J. L. Sessler, W. C. Dow, T. D. Mody, G. W. Hemmi, Y. Hao and R. A. Miller, *Proc. Natl. Acad. Sci. U.S.A.*, 1996, **93**, 6610-6615.
25. A. P. Thomas, P. Saneesh Babu, S. Asha Nair, S. Ramakrishnan, D. Ramaiah, T. K. Chandrashekar, A. Srinivasan and M. Radhakrishna Pillai, *J. Med. Chem.*, 2012, **55**, 5110-5120.
26. S. Young, K. Woodburn, M. Wright, T. Mody, Q. Fan, J. Sessler, W. Dow and R. Miller, *Photochem. Photobiol.*, 1996, **63**, 892-897.
27. M. Ethirajan, Y. Chen, P. Joshi and R. K. Pandey, *Chem. Soc. Rev.*, 2011, **40**, 340-362.
28. Y. Zhang, M. Jeon, L. J. Rich, H. Hong, J. Geng, Y. Zhang, S. Shi, T. E. Barnhart, P. Alexandridis, J. D. Huizinga, M. Seshadri, W. Cai, C. Kim and J. F. Lovell, *Nat. Nano.*, 2014, **9**, 631-638.
29. J. F. Lovell, C. S. Jin, E. Huynh, H. Jin, C. Kim, J. L. Rubinstein, W. C. Chan, W. Cao, L. V. Wang and G. Zheng, *Nat. Mater.*, 2011, **10**, 324-332.
30. B. Nikoobakht and M. El-Sayed, *Chem. Mater.*, 2003, **15**, 1957-1962.
31. J. V. Jokerst, A. J. Cole, D. Van de Sompel and S. S. Gambhir, *ACS Nano*, 2012, **6**, 10366-10377.

- 1
2 32. A. Needles, A. Heinmiller, P. Ephrat, C. Bilan-Tracey, A. Trujillo, C. Theodoropoulos, D. Hirson and F.
3 Foster, *IEEE Proceedings*, 2010, 390-393.
4 33. M. D. Abramoff, P. J. Magalhaes and S. J. Ram, *Biophoton. Intl.*, 2004, **11**, 36-42.
5 34. R. M. Mainardes and R. C. Evangelista, *Int. J. Pharm.*, 2005, **290**, 137-144.
6 35. A. J. Mieszawska, Y. Kim, A. Gianella, I. van Rooy, B. Priem, M. P. Labarre, C. Ozcan, D. P. Cormode, A.
7 Petrov and R. Langer, *Bioconjugate Chem.*, 2013, **24**, 1429-1434.
8 36. M. El Himri, A. Pastor and M. de la Guardia, *Fresenius' J. Anal. Chem.*, 2000, **367**, 151-156.
9 37. C. Fuller, J. Bargar, J. Davis and M. Piana, *Environ. Sci. Technol.*, 2002, **36**, 158-165.
10 38. A. C. Miller, M. Stewart, R. Rivas, S. Marino, G. Randers-Pehrson and L. Shi, *Radiation Meas.*, 2007, **42**,
11 1029-1032.
12 39. C. J. Orendorff and C. J. Murphy, *Journal of Physical Chemistry B*, 2006, **110**, 3990-3994.
13 40. S. Link, C. Burda, B. Nikoobakht and M. El-Sayed, *J. Phys. Chem. B.*, 2000, **104**, 6152-6163.
14 41. N. A. Smith, G. S. Cerefice and K. R. Czerwinski, *J. Radioanal. Nuc. Chem.*, 2013, **295**, 1553-1560.
15 42. C. Manfredi, V. Caruso, E. Vasca, S. Vero, E. Ventimiglia, G. Palladino and D. Ferri, *J. Solution Chem.*,
16 2006, **35**, 927-937.
17 43. S. Sant, V. Nadeau and P. Hildgen, *J. Control Release*, 2005, **107**, 203-214.
18 44. S. E. Bae, J. S. Son, K. Park and D. K. Han, *J. Control Release*, 2009, **133**, 37-43.
19 45. Y. Yang, N. Bajaj, P. Xu, K. Ohn, M. D. Tsifansky and Y. Yeo, *Biomaterials*, 2009, **30**, 1947-1953.
20 46. G. Hong, Y. Zou, A. L. Antaris, S. Diao, D. Wu, K. Cheng, X. Zhang, C. Chen, B. Liu and Y. He, *Nat. Comm.*,
21 2014, **5**.
22 47. J. Feitelson and D. Mauzerall, *J. Phys. Chem.*, 1996, **100**, 7698-7703.
23 48. E. Voigtman, A. Jurgensen and J. Winefordner, *Anal. Chem.*, 1981, **53**, 1442-1446.
24 49. H. Zhang, B. Zhang, M. Zhu, S. M. Grayson, R. Schmehl and J. Jayawickramarajah, *Chem. Commun.*, 2014,
25 **50**, 4853-4855.
26
27
28
29
30
31
32
33
34
35
36
37
38
39
40
41
42
43
44
45
46
47
48
49
50
51
52
53
54
55
56
57
58
59
60

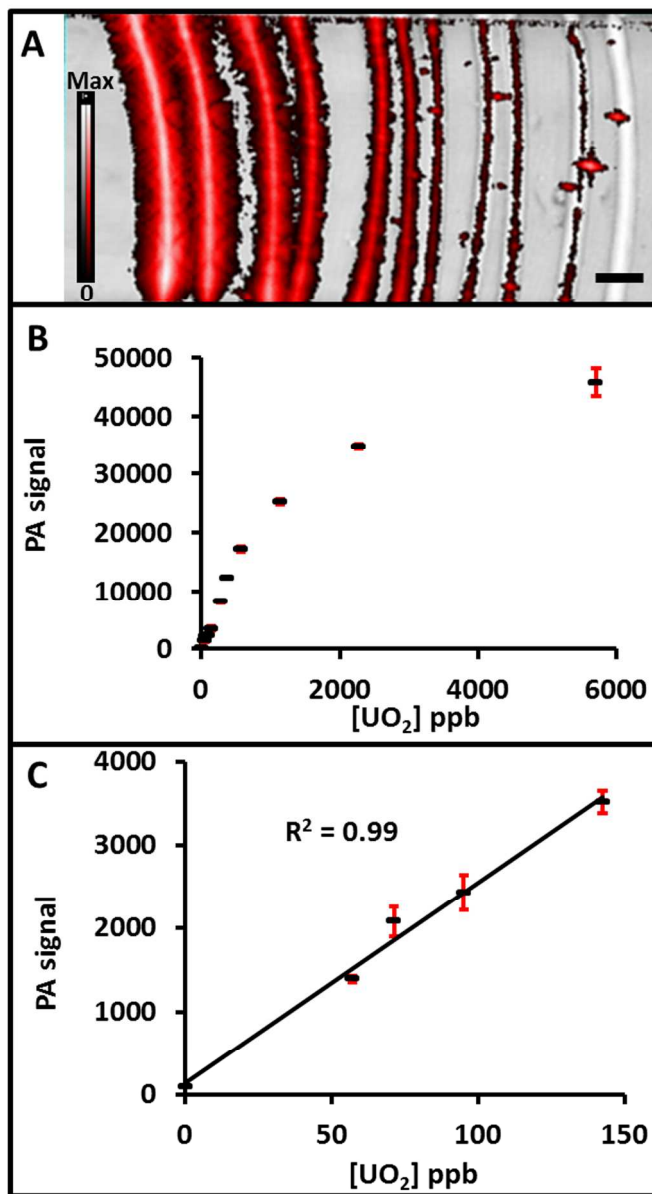


123x85mm (300 x 300 DPI)



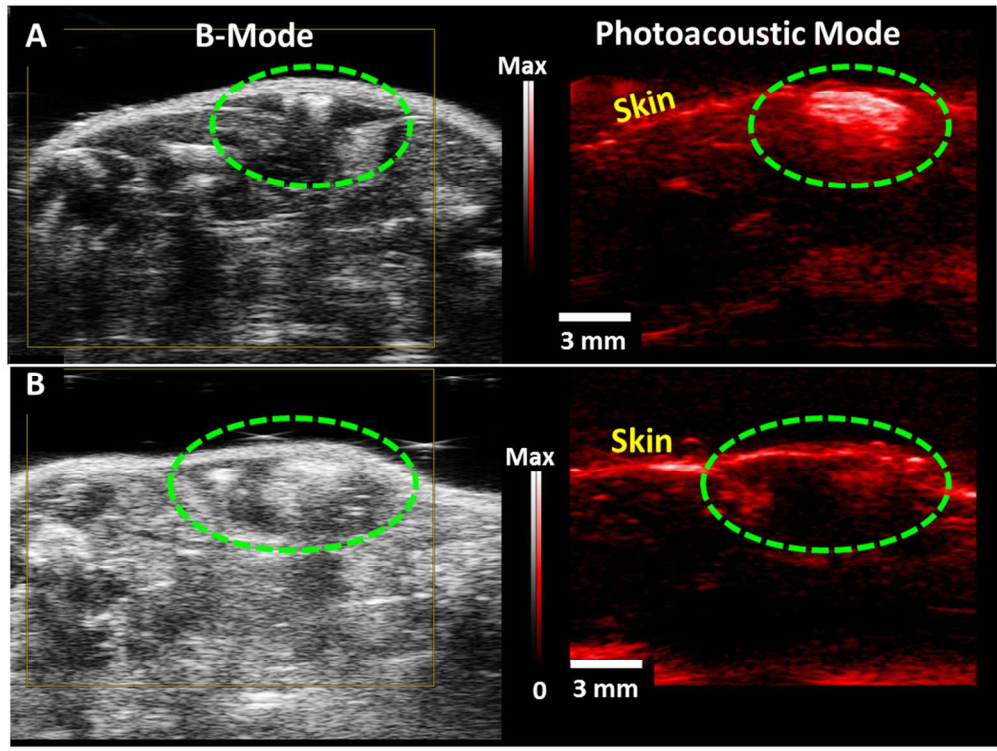
105x125mm (300 x 300 DPI)

1
2
3
4
5
6
7
8
9
10
11
12
13
14
15
16
17
18
19
20
21
22
23
24
25
26
27
28
29
30
31
32
33
34
35
36
37
38
39
40
41
42
43
44
45
46
47
48
49
50
51
52
53
54
55
56
57
58
59
60

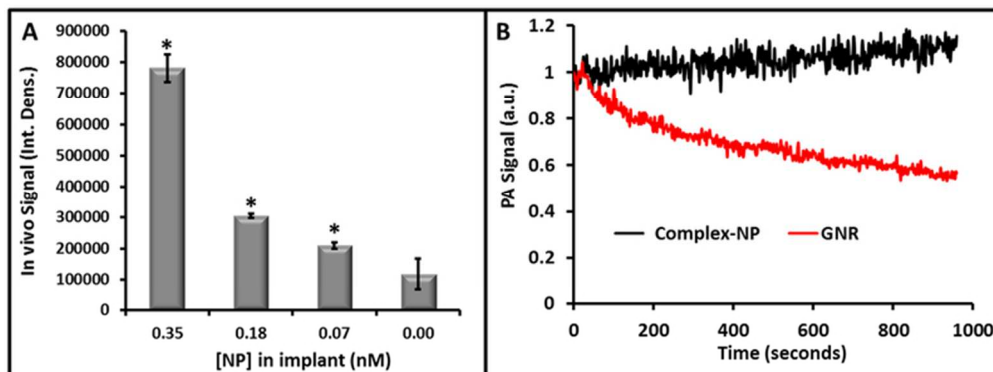


158x281mm (300 x 300 DPI)

1
2
3
4
5
6
7
8
9
10
11
12
13
14
15
16
17
18
19
20
21
22
23
24
25
26
27
28
29
30
31
32
33
34
35
36
37
38
39
40
41
42
43
44
45
46
47
48
49
50
51
52
53
54
55
56
57
58
59
60



134x101mm (300 x 300 DPI)



67x25mm (300 x 300 DPI)